Atomically dispersed Pt (II) on WO₃ for highly selective sensing and catalytic oxidation of triethylamine

Fubo Gu[a,b,c], Yuzhen Cui[a,b], Dongmei Han[a,b], Song Hong[a,b], Maria Flytzani-Stephanopoulos[c], Zhihua Wang[a,b,*]

[a] State Key Laboratory of Chemical Resource Engineering, Beijing University of Chemical Technology, Beijing 100029, China
[b] Beijing Advanced Innovation Center for Soft Matter Science and Engineering, Beijing University of Chemical Technology, Beijing 100029, China
[c] Department of Chemical and Biological Engineering, Tufts University, Medford, Massachusetts 02155, USA

ABSTRACT

Triethylamine is a volatile organic compound and harmful to the environment. Development of an efficient detection and conversion method for triethylamine becomes urgent. In this work, Pt loaded three-dimensionally ordered macroporous (3DOM) WO₃ materials were successfully synthesized through a colloidal crystal template method. Compared to Pt clusters on the surface, atomically dispersed Pt (II) on WO₃ increased the number of active sites and decrease the activation energy, which resulted in highly efficient oxidation and high sensitivity detection of triethylamine. The sensor based on the 3DOM SA-Pt/WO₃ with atomically dispersed Pt (II) exhibited super high sensitivity (28.37 ppm^{-1}) and ultra-low detection limit (0.18 ppb) to triethylamine. The high selectivity possibly originated from the selective adsorption of triethylamine from other volatile organic compounds on the uniform single atom Pt (II) sites.

1. Introduction

Triethylamine (TEA), as a volatile organic compound with intense ammonia smell, is extensively used in the organic solvent [1], curing agent [2], catalyst [3], preservative [4], and so on. TEA is prone to environmental hazards due to its volatility, flammability and explosive properties. Because of its toxicity, long-term exposure to TEA can cause headaches, pulmonary edema, gastroenteritis and other health problems [5]. According to the recommendations of the National Institute for Occupational Safety and Health Administration, the environmental concentration of TEA should be lower than 10 ppm [6]. In addition, studies have shown that species such as fish and shellfish can release volatile amines such as TEA and trimethylamine (TMA), and the concentration gradually increases with the decreasing fish freshness [7,8]. In this sense, TEA and TMA can be used as chemical markers to monitor fish freshness. Although many researchers have reported on TEA detection over the years, there still are issues such as low sensitivity and poor selectivity which limit their applications. Hence, more research effort is needed for the design and development of high-performance TEA sensors.

Metal oxide semiconductor (MOS) sensors are portable, low power and remotely operated detection devices, and the sensing mechanism is based on the redox reaction between adsorbed oxygen and target molecules. O₂ molecules from the air capture electrons from the conduction band of MOS and form adsorbed oxygen. When the MOS is exposed to target molecules, the reaction between adsorbed oxygen and target molecules takes place, which will release the electron and result in resistance change of the MOS sensor. Recently, high sensitivity and high selectivity detection of target gases by the MOS sensors have been reported by novel strategies, such as atomic layer deposition and metal−organic framework nanomembrane coating [9,10]. Among diverse MOS including WO₃ [11–19], ZnO [20,21], TiO₂ [22], In₂O₃ [23,24], and NiO [25], WO₃, a n-type semiconductor with low band-gap, has superior charge transport capability [26–33], which will increase the signal-to-noise ratio of the sensor and benefit its practical application [34,35]. In addition, three-dimensionally ordered macroporous (3DOM) structures are promising candidates as gas sensing materials. Their well-connected channels and ordered macroporous structure are advantageous to the interaction between sensing materials and gas molecules [36,37]. Therefore, the superior conductivity and structure make 3DOM WO₃ a promising sensing material among MOS sensors.

Precious metals are widely used to optimize the sensing properties of MOS sensors due to their excellent catalytic activity [38–40]. Atomic dispersion can maximize the exposure of precious metal atoms and

---

* Corresponding author.
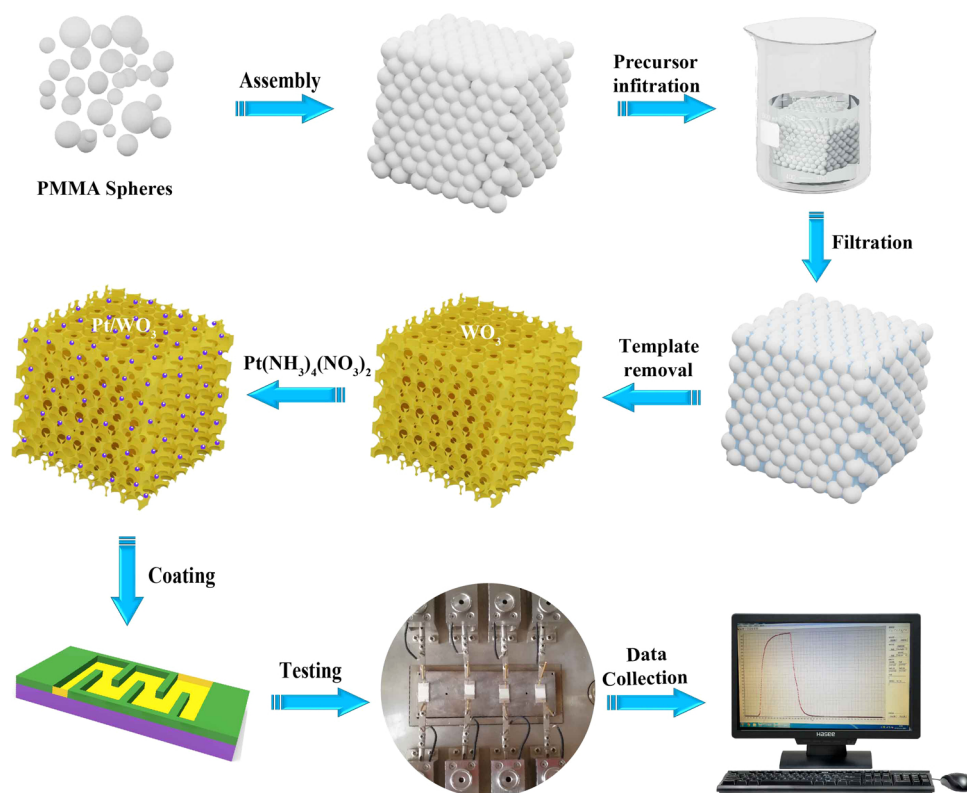 E-mail address: zhwang@mail.buct.edu.cn (Z. Wang).

Fig. 1. Schematic illustration of the experimental procedure.

increase their utilization [41–51]. Moreover, atomically dispersed precious metals may benefit the enhancement of selectivity due to the specific active sites which ensure uniform adsorption of reactant molecules. Wang et al. have reported a Rh/CoO single atom catalyst for olefin hydroformylation, which exhibits high selectivity for linear products [52]. Lucci et al. prepared a Pt/Cu single-atom alloy catalyst which exhibited high activity and selectivity for butadiene hydrogenation to butene [53]. In this work, a TEA sensor based on the atomically dispersed Pt (II) on 3DOM WO_3 is first reported. Due to a high number of the specific isolated Pt (II) active sites, the synthesized 3DOM SA-Pt/WO_3 exhibits low activation energy for the oxidation of TEA, which was accompanied by a significant resistance change of SA-Pt/WO_3.

2. Experimental

2.1. Preparation of 3DOM WO_3 and Pt loaded 3DOM WO_3

Fig. 1 shows the schematic illustration of the experimental procedure.

The purities, CAS numbers and providers of all the used chemicals were shown in Table S1. 3DOM WO_3 were prepared via a modified colloidal crystal template method [54,55]. The templates were ordered PMMA microspheres (330 ± 3 nm) and their scanning electron microscopy (SEM) image is shown in Fig. S1. The typical preparation process for 3DOM WO_3 was as follows: 3.37 g $(NH_4)_6W_7O_{14}\cdot5H_2O$ was added to a mixed solution of methanol and deionized water (3 mL each), and then stirred at room temperature for 30 min. Subsequently, a certain amount of citric acid was added (the molar ratio to W was 1.25:1) to the solution and continue to stir for 1 h to obtain a precursor solution. 1.25 g PMMA templates were added to the precursor solution, and immersed for 4 h at room temperature, and then a white intermediate product was obtained after vacuum filtration. The above product was dried at room temperature, and then the powder was placed in a ceramic boat, calcined in a tube furnace at 475 °C for 3 h with an air

flow rate of 100 mL/min (heating rate 1 °C/min). The templates were removed and then cooled to room temperature to obtain yellow WO_3 powders.

Pt loaded 3DOM WO_3 (Pt/WO_3) were prepared by a reduction method using tetraammine platinum (II) nitrate as a precursor with ethylene glycol and methanol as solvents. In a typical synthesis procedure of Pt loaded 3DOM WO_3, 0.20 g yellow WO_3 powders were added in 40 mL ethylene glycol with stirring for 15 min and then an appropriate amount of tetra ammine platinum (II) nitrate solution was added with stirring for 30 min. Subsequently, a certain amount of 100 mM $NaBH_4$ solution (Pt/$NaBH_4$ molar ratio of 1:10) was quickly added and the mixture was stirred for another 30 min. After vacuum filtration, the powders were placed in a vacuum oven at 60 °C. The prepared sample with atomically dispersed Pt (II) was named as SA-Pt/WO_3. We also use methanol to replace ethylene glycol as the solvent and the obtained sample with Pt nanoclusters was named as NC-Pt/WO_3.

2.2. Characterization studies

The crystalline phases of the sensing materials were determined by X-ray diffraction (XRD, Bruker-D8 Advance) using Cu Kα radiation. The range was from 5° to 90° at a rate of 10° min^{-1}. Raman spectra (LabRAM Aramis, HORIBA) were recording with a He-Ne laser (excitation wavelength: 532 nm), and wavelength range is 100 to 1000 cm^{-1}. The morphologies and structures of the synthesized samples were imaged by SEM (Hitachi S-4700) and aberration-corrected high angle annular dark-field scanning transmission electron microscopy (ac-HAADF-STEM, JEOL JEM-ARM200 F). Surface composition and chemical binding energy were identified by X-ray photoelectron spectroscopy (XPS, VG Scientific ESCALAB 250X). Elemental composition was determined on a Shimadzu ICPS-7500 inductively coupled plasma atomic emission spectrometer (ICP-AES). The experimental process for ICP test is as follows:100 mg samples were dispersed in 5 mL of aqua regia with ultrasonic for 3 h, then soaking for 24 h. The insoluble matter

was separated before the ICP test, and the average value was calculated after three independent tests. N_2 adsorption-desorption isotherms were obtained on a Micromeritics ASAP 2026 analyzer. The surface area was measured using the Brunauer-Emmett-Teller (BET) method. The electrical properties were recorded in the Hall effect measurement system (RH2030, Phys Tech). UV-vis spectrophotometer (SHIMADZU UV-2600) was used to analyze the optical properties of the samples, and $BaSO_4$ was used for baseline correction. Diffuse reflectance infrared Fourier transform spectroscopy using CO as a probe molecule (CO-DRIFTS) was conducted on Nicolet iS50 FTIR spectrometer. The samples were pretreated in He (50 mL/min) in the DRIFTS cell at 240 °C for 30 min. Then CO was adsorbed until saturation coverage by flowing 10% CO/He (50 mL/min). After that, the system was purged with He (50 mL/min) for 30 min to remove any gas-phase CO before DRIFTS measurements. For CO temperature-programmed reduction (CO-TPR), the samples were pretreated in 1% O_2/He (50 mL/min) at 300 °C for 30 min and then cooled to 40 °C. After purging with He, the TPR profiles were obtained from 40 °C to 600 °C in 3% CO/He (50 mL/min) at a heating rate of 10 °C/min. On-line Mass spectrometer was used to analyze the exhaust gas.

2.3. Performance testing

A certain amount of obtained product was uniformly dispersed in ethanol and ground to form a paste in an agate mortar. Subsequently, the paste was coated on an Ag-Pd interdigitated electrode. After the evaporation of ethanol at room temperature, the fabricated sensors were aging at 300 °C for 12 h in air. A CGS-4TPs intelligent gas sensing instrument (Beijing Elite Tech Co., Ltd) was used to test the performance of the prepared sensors. The relative environment humidity during the test was maintained at 25 ± 5%. In this work, the ratio of Ra (resistance in the air) to Rg (resistance in target gas) is defined as the response. The time required to reach 90% of the total resistance change during adsorption and desorption were defined as response and recovery time. For fish freshness monitoring, a certain amount of Carassius auratus pieces was put into a sealed container with a capacity of 1.5 L, and then placed in an oven at 25 °C. 100 mL of gas was taken every 2 h, used for analyzing the degree of fish spoilage.

3. Results and discussion

3.1. Structural and morphological characterization of the samples

XRD was used to characterize the crystallographic structures of WO_3, NC-Pt/WO_3, and SA-Pt/WO_3, and all the diffraction peaks of the XRD patterns (Fig. S2) can be well indexed to monoclinic WO_3 (PDF. 43-1035). No other peaks are observed indicating high purity of the samples. The EDS patterns (Fig. S3) also indicate the existence of W, O and Pt elements in the samples. No diffraction peaks of Pt or PtO_2 can be found to the samples, that may result from low content and high dispersion of Pt [56]. Table 1 shows the crystal structures, lattice constants, and strains of the samples. The crystallite sizes (D) are estimated by Debye-Scherrer Eq. (1):

$$D = k\lambda/\beta cos\theta \qquad (1)$$

Table 1
Structural parameters of the samples.

Samples	D (nm)	Lattice parameter			Lattice strain ε (%)
		a (Å)	b (Å)	c (Å)	
WO_3	15.476	7.316	7.483	7.638	0.963
SA-Pt/WO_3	17.334	7.346	7.527	7.680	0.903
NC-Pt/WO_3	17.441	7.313	7.529	7.671	0.919

k, λ, and β represent the Scherrer constant, X-ray wavelength and full width at half maximum (FWHM), respectively, and θ is the diffraction angle of the peak. The microstrain (ε) is determined by Eq. (2):

$$\varepsilon = \beta/4 \tan\theta \qquad (2)$$

There is no significant difference between WO_3 and Pt-loaded WO_3, which indicates that Pt is only supported on the surface and has almost no effect on the crystal structure of WO_3. Therefore, we can reasonably surmise that Pt is not doped in the lattice of WO_3. Raman spectra of the products are shown in Fig.2a. The strong peaks at 804 cm^{-1} and 707 cm^{-1} are assigned to W—O—W symmetric and asymmetric stretching frequencies. The W—O—W bending vibration of bridging oxygen results in the appearance of a strong peak at 267 cm^{-1} and the weak peak at 323 cm^{-1} [57]. The peaks at 804 cm^{-1}, 707 cm^{-1} and 267 cm^{-1} are typical characteristics of monoclinic WO_3 [58], which is consistent with the XRD results.

More detailed information about the chemical states of W, O, and Pt was obtained by XPS. W^{6+} and W^{5+} can be obtained by the Gauss fitting curves of W 4f spectra. The peaks with binding energies of ∼37.34 eV and ∼35.22 eV correspond to W^{5+}, and the peaks of ∼37.65 eV and ∼35.61 eV correspond to W^{6+} (Fig. S4a). The relative contents of W^{5+} to W^{6+} are listed in Table 2, and the Pt-loaded 3DOM samples, especially SA-Pt/WO_3, showed the highest W^{5+}/W^{6+} value, indicating SA-Pt/WO_3 has the highest number of defects. The content of W^{5+} can indirectly reflect the concentration of oxygen vacancy [59], so we surmise that SA-Pt/WO_3 has the highest number of oxygen vacancies. The existence of oxygen vacancies benefits the formation of adsorbed oxygen. Oxygen-related peaks can be assigned to three oxygen species (Fig. S4b): lattice oxygen (O_{latt})at ∼530.30 eV, deficient oxygen (O_{def}) at ∼531.62 eV and adsorbed oxygen (O_{ads}) at ∼533.12 eV [60,61]. The relative contents of oxygen species are summarized in Table 2, and SA-Pt/WO_3 has the most adsorbed oxygen, which will improve its gas sensitivity [62]. This will be discussed in detail later. Fig. 2b shows the XPS of Pt 4f and it is clear that Pt is mainly in the form of Pt^{2+} on the WO_3 surface. A weak peak of metallic Pt can be seen in NC-Pt/WO_3, indicating the existence of Pt clusters. The surface contents of Pt are shown in Table 3. It can be seen from the table that the contents of Pt are higher than the ICP results because XPS is a surface analysis method. In addition, the content of Pt in NC-Pt/WO_3 is higher than that in SA-Pt/WO_3 because Pt (II) is reduced deeply when using methanol as solvent.

Highly sensitive CO-DRIFTS was used for detecting the structure and bonding environment of Pt [63,64]. Fig. 2c shows the CO-DRIFT spectra of SA-Pt/WO_3 and NC-Pt/WO_3. The absorption peaks at 2145 cm^{-1} (2139 cm^{-1}), 2112 cm^{-1} and 2094 cm^{-1} (2086 cm^{-1}) are indexed to the oxidized Pt (Pt_{ox}), isolated Pt atom (Pt_{iso}) and metallic Pt cluster (Pt_m), respectively [65]. The absorption wavenumbers of NC-Pt/WO_3 are different from SA-Pt/WO_3. SA-Pt/WO_3 has a sharp and strong absorption peak at 2112 cm^{-1}, indicating the existence of lots of Pt_{iso}. The 2112 cm^{-1} peak of NC-Pt/WO_3 is not clearly seen because the Pt_m absorption peak overlaps with Pt_{iso} peak, resulting in a 2086 cm^{-1} peak. The Pt_m peak of NC-Pt/WO_3 has a large FWHM, which indicates the existence of different sizes Pt clusters due to the deeply reduced of Pt precursor. The CO absorption wavenumbers of Pt_{ox} to NC-Pt/WO_3 and SA-Pt/WO_3 are 2145 cm^{-1} and 2139 cm^{-1}, and the shift in absorption position is due to the difference in Pt states and CO coverage.

The nitrogen adsorption-desorption isotherms (Fig. S5) were used to analyze the specific surface areas and porous structure characteristics of the products. All the samples display a type II and IV combination isotherm with an H3 type hysteresis loop. When the relative pressure (p/p_0) is below 0.9, the nitrogen adsorption amounts increase slowly. When above 0.9, the nitrogen adsorption amounts increase significantly. The results indicate that the samples have a 3DOM structure [66,67]. The specific surface areas of WO_3, SA-Pt/WO_3 and NC-Pt/WO_3 are shown in Table 3, no significant change is observed among the
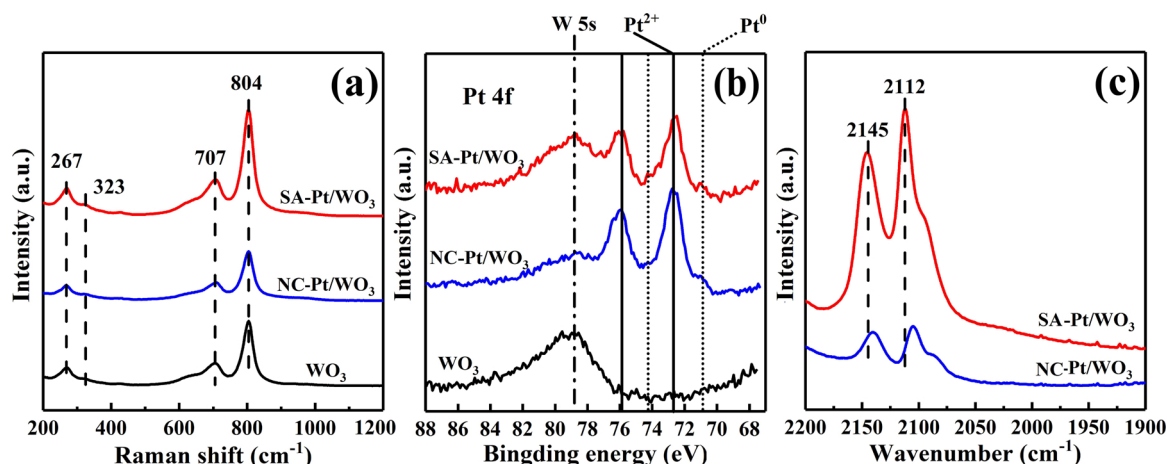
Fig. 2. (a) Raman and (b) Pt 4f XPS spectra of WO_3, NC-Pt/WO_3 and SA-Pt/WO_3, (c) CO-DRIFTS spectra of NC-Pt/WO_3 and SA-Pt/WO_3.

Table 2
Surface chemical composition of the samples.

Samples	Surface element relative contents		
	W^{5+}/W^{6+}	O_{def}/O_{latt}	O_{ads}/O_{latt}
WO_3	0.56	0.21	0.11
SA-Pt/WO_3	0.61	0.25	0.17
NC-Pt/WO_3	0.59	0.23	0.15

samples.

Fig. 3a, S6 and S7a show the SEM images of SA-Pt/WO_3, WO_3, and NC-Pt/WO_3. As expected, all products exhibit a highly ordered macroporous structure that is obtained by long-range ordered and densely packed PMMA templates. The pore diameter and wall thickness are 200 ± 5 and 20 ± 2 nm, respectively. Interconnected macropores will facilitate gas diffusion and improve gas sensing performance. It is shown that the macroporous structure is not destroyed during the loading of Pt. Fig. 3b and S7b are the STEM images of SA-Pt/WO_3 and NC-Pt/WO_3, which also show the porous structures. Fig. 3c depicts the STEM-EDS elemental mapping diagrams of SA-Pt/WO_3. It can be clearly seen that the W, O, and Pt elements are evenly distributed. Fig. 3d and Fig. S7c are the HAADF-STEM images of SA-Pt/WO_3 and NC-Pt/WO_3. Pt is mainly present in single atoms and sub-nm clusters. Inset of Fig. 3d indicates nearly 80% Pt is present as isolate atoms on SA-Pt/WO_3. Compared to SA-Pt/WO_3, the Pt dispersion on NC-Pt/WO_3 is inferior, and Pt exists in various states such as single atoms, clusters, and nanoparticles due to the deep reduction when using methanol as solvent (as shown in Fig. S7d). These findings are consistent with the DRIFTs results.

The SA-Pt/WO_3 and NC-Pt/WO_3 were further investigated by CO-TPR, and the results are shown in Fig. S8. The TPR curves show two strong peaks at 220 °C and 440 °C for NC-Pt/WO_3 and at 300 °C and

440 °C for SA-Pt/WO_3. The peak at 440 °C can be attributed to the reduction of WO_3 to WO_x [68,69]. The peaks at 220 °C and 300 °C correspond to the reduction of cationic Pt (II) and the reduction temperature of SA-Pt/WO_3 is higher than that of NC-Pt/WO_3 because of the stronger interaction between Pt_{iso} and WO_3.

The UV–vis spectra of the as-prepared WO_3, SA-Pt/WO_3, and NC-Pt/WO_3 are shown in Fig. S9. The transfer of electrons from the valence band to the conduction band lead WO_3 has an obvious absorption in the UV region with a wavelength of ~ 340 nm. The absorption wavelength of Pt loaded WO_3 is shifted to 350 nm. The forbidden bandwidths (Eg) of WO_3, NC-Pt/WO_3, and SA-Pt/WO_3 are 3.06, 3.01 and 2.98 eV, respectively. The Eg value of pure WO_3 is higher than those of other samples, indicating that the Pt modification can effectively reduce the band gap and the electron transfer energy. In addition, the Eg values of the Pt-loaded samples are also different, probably because of the different interaction between Pt and WO_3. SA-Pt/WO_3 has the smallest band gap because Pt exists in single atoms, which have a strong interaction with WO_3. This result is consistent with the CO-TPR results. Strong interaction between Pt_{iso} and WO_3 increases the reduction temperature of cationic Pt (II). Both CO-TPR and UV results indicate that the atomically dispersed Pt (II) increases the interaction between Pt and WO_3 [70].

3.2. Sensing performance

The sensing response process is based on the redox reaction between adsorbed oxygen and target molecules. The reaction temperature (i.e., operating temperature for the sensor) must be high enough to get the good activity of the catalyst (i.e., sensing material). Therefore, the sensing performance of a sensor is closely related to the operating temperature. When the operating temperature is relatively low, the activity of the sensing materials and the conversion rate of target molecules are lower. However, adsorbed oxygen and target molecules will

Table 3
Composition, special surface area and sensing properties of the samples.

Samples	Pt content[a] (wt%)	Pt content[b] (wt%)	Surface area (m²/g)	Sensitivity[c]	LOD[c] (ppb)
WO_3	–	–	17.80	0.84	31.37
NC-Pt/WO_3	3.71	0.57	19.04	17.33	0.76
SA-Pt/WO_3	1.27	0.22	19.63	28.37	0.18

[a] Determined by XPS.
[b] Determined by ICP.
[c] Sensitivity (ratio of response to gas concentration) and limit of detection (LOD) were calculated according the response of the sensors at the optimum operating temperature of 240 °C.
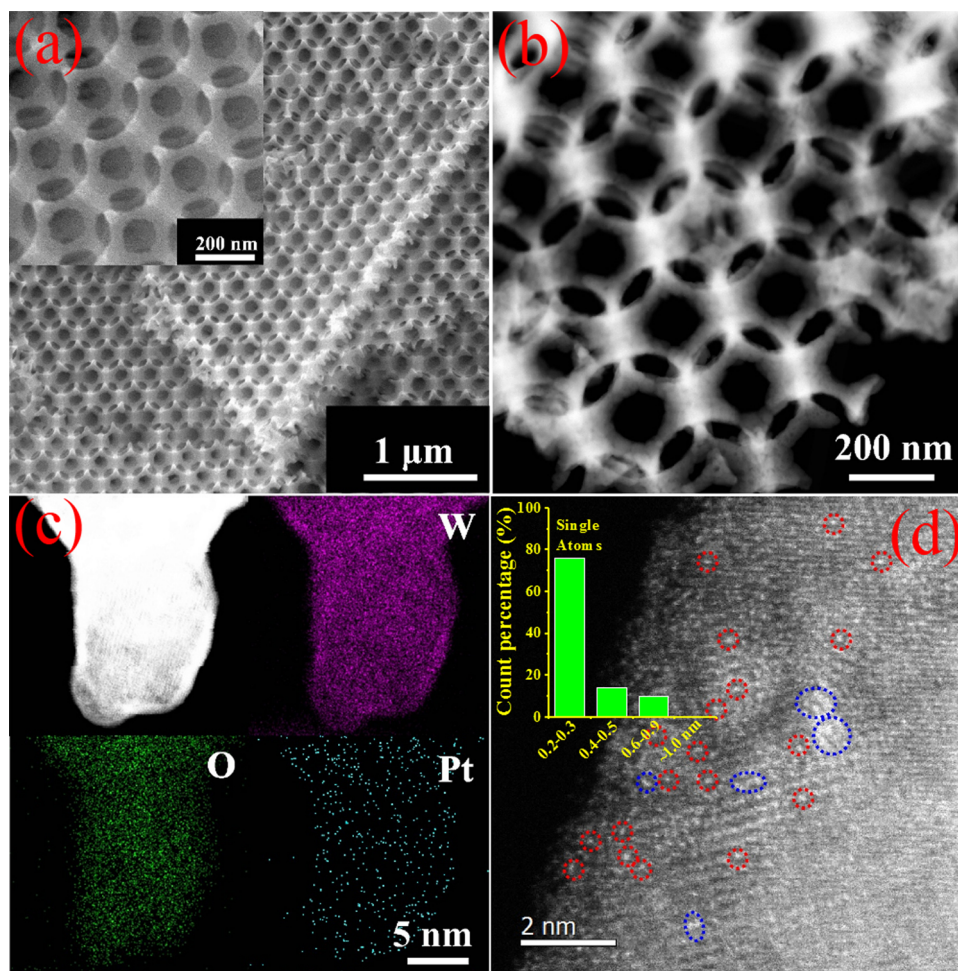
Fig. 3. (a) SEM images (inset is the image with high magnification), (b) STEM image, (c) STEM-EDS elemental mapping images and (d) ac-HAADF-STEM image of SA-Pt/WO₃ (atomically dispersed Pt species and sub-nm clusters are marked with red and blue circles, and the inset is the size distribution based on over 100 Pt species) (For interpretation of the references to colour in this figure legend, the reader is referred to the web version of this article).

desorb from the surface of the sensing materials at relatively high operating temperature. Therefore, there is an adsorption-desorption balance to reach the maximum response at the optimum operating temperature. The response of the fabricated sensors to 50 ppm TEA at the test temperature of 180 °C to 280 °C is shown in Fig. S10. For all the sensors, the response gradually increases with increasing temperature, and then reaches a maximum at the optimum operating temperature. After that, the response gradually decreases. The Pt-loaded 3DOM WO₃ sensor shows better performance compared to the WO₃ sensor. In particular, SA-Pt/WO₃ has the highest response of 1182 ± 57, ~30 times higher than WO₃. Moreover, the optimum operating temperature of WO₃ is 260 °C, while it is decreased to 240 °C for the Pt-loaded sensors, which indicates that the Pt modification can reduce the operating temperature and improve the gas sensing performance. Compared to the literature (Table S2), the SA-Pt/WO₃ sensor showed a much higher response and lower operating temperature for TEA detection.

Apparent activation energies can be calculated from the resistance changes of SA-Pt/WO₃ and NC-Pt/WO₃ at different operating temperatures at 50 ppm TEA (shown in Fig. 4a and 4b). Arrhenius-type plots for the rate of resistance change ($|dR|/dt$) and the temperature (T) are shown in Fig. 4 c and d. As shown in Fig. 4c and 4d, *Ea* can be obtained from the slope of $\ln(|dR|/dt) \sim 1/T$. The values of *Ea* are 10.73 and 17.62 kJ/mol for SA-Pt/WO₃ and NC-Pt/WO₃, respectively. Both Ea values are relatively low, indicating an adsorption-limited reaction. Still, the *Ea* value of SA-Pt/WO₃ is smaller than NC-Pt/WO₃, which means that higher activity of SA-Pt/WO₃ is expected at the low-

temperature regime.

The sensing response of the sensor is also closely related to the TEA concentration. The relationship between response and gas concentration can be empirically expressed as Eq. 3:

$$R_g = 1 + A_g C_g^{\beta} \tag{3}$$

or

$$\log(R_g - 1) = \log A_g + \beta \log C_g \tag{4}$$

where R_g is the response, A_g is a prefactor, C_g is gas concentration and β is the exponent on C_g, which mainly depends on the surface oxygen species and the microstructure of the sensing materials. The Log $(R_g - 1)$ to Log C_g curves of the sensors to TEA are shown in Fig. 5. The responses of the sensors increase with the TEA concentrations. The β values of WO₃, SA-Pt/WO₃, and NC-Pt/WO₃ are 0.88, 1.06 and 0.99, respectively. The relatively close to 1 resulting from the similar regular macroporous structure of WO₃ in all samples, as shown in the SEM images (Fig. 3a and Fig. S6, S7a). The β values of SA-Pt/WO₃ and NC-Pt/WO₃ are a little bit higher because of the existence of Pt, which can lead to the change of the microstructure and the different reaction mechanism.

The sensitivity of the sensors is the ratio of response to gas concentration, which can be obtained by fitting the slope of the straight line. As shown in Fig. 6a and Table 3, the sensitivities are 0.84 ppm⁻¹, 17.33 ppm⁻¹ and 28.37 ppm⁻¹ for WO₃, NC-Pt/WO₃ and SA-Pt/WO₃, respectively. The limits of detection (LOD) of the sensors are shown in
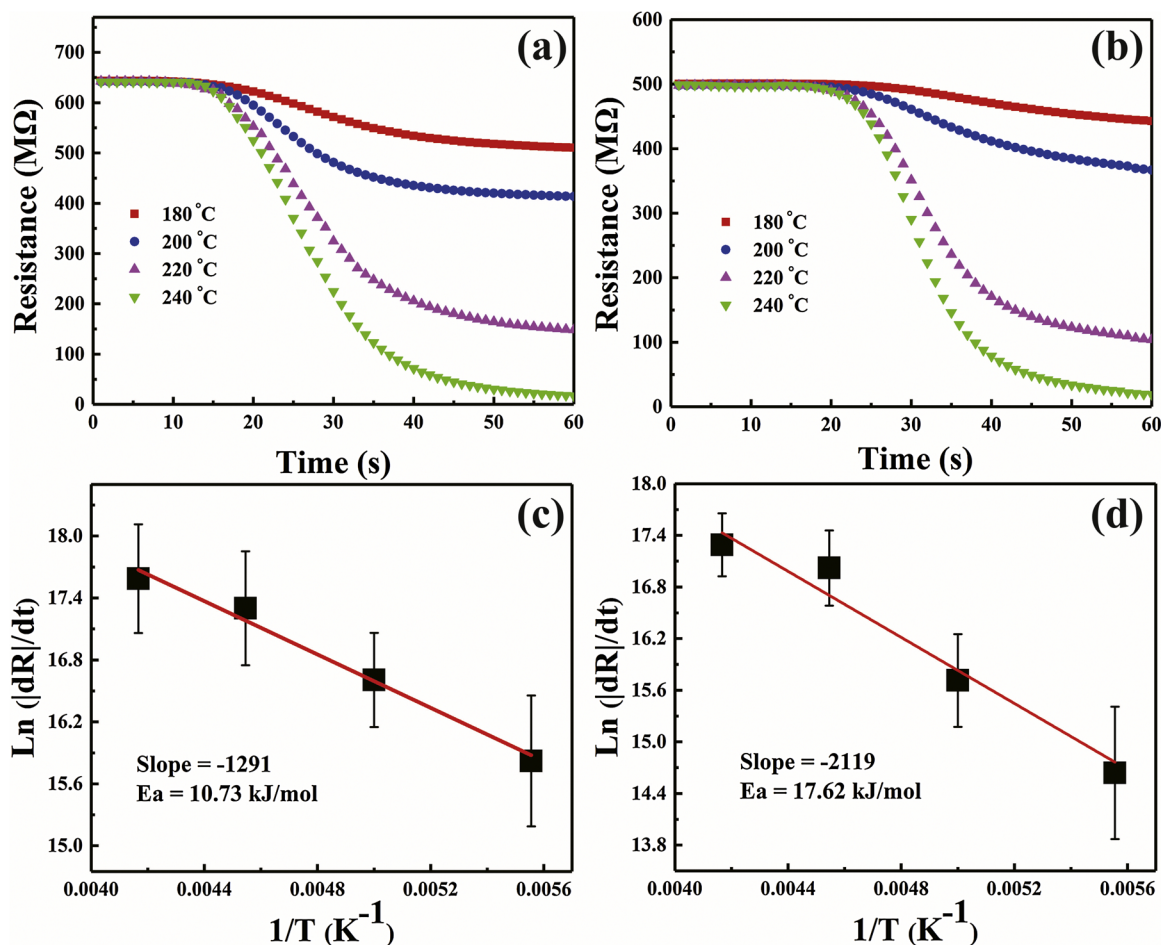
Fig. 4. The resistance changes of SA-Pt/WO₃ (a) and NC-Pt/WO₃ (b) at different temperatures to 50 ppm TEA, (c) and (d) Arrhenius-type plots for the rate of change of the resistance with temperature for SA-Pt/WO₃ and NC-Pt/WO₃ (activation energies were calculated by three measurements).
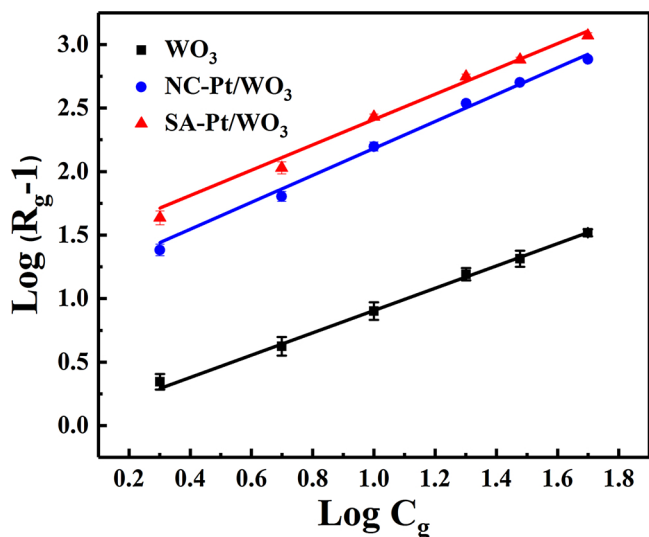

Fig. 5. Log ($R_g - 1$) vs Log C_g curves of WO₃, NC-Pt/WO₃ and SA-Pt/WO₃.

Table 3. The detailed calculation method of LOD and the baseline information (Fig. S11 and Table S3) before exposure to TEA are shown in the Supplementary Information [71–73]. The WO₃ sensor has the highest LOD value of 31.37 ppb. The LOD of Pt-modified sensor is significantly reduced. The NC-Pt/WO₃ sensor's LOD is 0.76 ppb. The SA-Pt/WO₃ sensor has the lowest LOD of 0.18 ppb. We also studied the gas

sensitivity of the SA-Pt/WO₃ sensor to TMA. Fig. S12 shows the test results of the EG-Pt/WO₃ sensor for TMA. The sensitivity and LOD for TMA are 5.52 ppm⁻¹ and 0.91 ppb. In addition, as shown in Fig. 6b, the response for TEA and TMA are higher than those of other gases, which indicates the SA-Pt/WO₃ sensor has an excellent selectivity.

Fig. 7a shows the four-cycle response curve of SA-Pt/WO₃ to 50 ppm TEA. It can be seen that the sensor has excellent repeatability. The response of the SA-Pt/WO₃ remains stable after 4 weeks of continuous testing (as shown in Fig. 7b), indicative of the good stability of the sensor. Fig. S13 shows the response/recovery time of the SA-Pt/WO₃ sensor is 20 s/253 s. The effect of humidity on the performance of the SA-Pt/WO₃ sensor is shown in Fig. S14. Under a relative humidity of 20–30%, the response of the sensor to 50 ppm TEA is not significantly affected. The high sensitivity, high selectivity, and rapid response indicate that the SA-Pt/WO₃ sensor would be a good candidate for low concentration TEA detection.

The fabricated sensors were used to monitor fish freshness. We investigated the response change with storage time to 200 g Carassius auratus. As can be seen from Fig. S15a, SA-Pt/WO₃ has the highest response among the three sensors. In addition, the fish decay rate increases after storage for 6 h. When the storage time reaches 12 h, the response value of the SA-Pt/WO₃ sensor increases to 65. Fig. S15b shows the response to the quantities of Carassius auratus with the same storage time of 12 h. The concentration of spoiled gas increased with fish quantity. SA-Pt/WO₃ has the highest response to different fish quantities among the three sensors. Fig. S16 is the response/recovery curve of the SA-Pt/WO₃ sensor to the gas from 200 g Carassius auratus after 12 h. The response/recovery time is 22 s and 103 s. These results
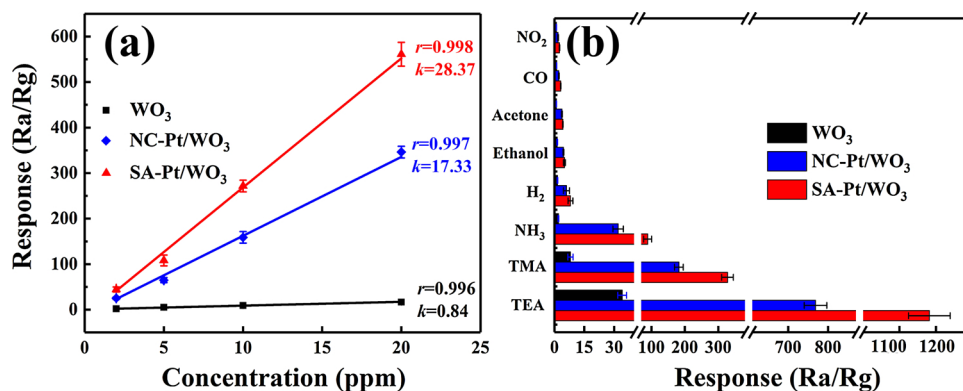
indicate that SA-Pt/WO$_3$ has a promising application in rapid fish freshness monitoring through the catalytic conversion of TEA and TMA.

3.3. Catalytic and sensing mechanism

The sensing mechanism is based on the redox reaction between adsorbed oxygen and TEA molecules. In the air, O$_2$ molecules obtain electrons form the conduction band of WO$_3$ and from adsorbed oxygen. The species of adsorbed oxygen can be determined according to Eq. 3, where the β values (the slope of the curve in Fig. 5) depend on the charged state of the adsorbed oxygen [74,75]. When the value is 0.5, the absorbed oxygen should be O^{2-}, and when the value is 1, adsorbed oxygen is O- [74,76]. The β values of WO$_3$, SA-Pt/WO$_3$, and NC-Pt/WO$_3$ are relatively close to 1. Therefore, the adsorbed oxygen on the sensor surface is O$^-$.

After the electrons are captured, a depletion layer is formed in WO$_3$ and the resistance of the sensor will increase. The chemical reaction is as follows:

$$O_2(gas) + 2e^- \rightarrow 2O^-(ads) \tag{5}$$

When the sensor is exposed to TEA, TEA will be completely oxidized and the reaction between O$^-$ and TEA can be described as Eq. 6 [77]:

$$2(C_2H_5)_3N + 43O^-(ads) \rightarrow 12CO_2 + 15H_2O + 2NO_2 + 43e^- \tag{6}$$
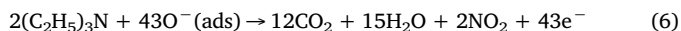
After the reaction, the captured electrons will be released to WO$_3$, thereby reducing the depletion layer thickness which means the decrease of the sensor resistance [78]. The sensing mechanism is shown schematically in Fig. 8. As shown in the DRIFTS of SA-Pt/WO$_3$, there is a sharp and strong absorption peak at 2112 cm^{-1}, which indicates Pt$_{iso}$ sites have a homogeneous local environment [64]. High electron donating TEA molecules will be selectively absorbed on the uniform Pt$_{iso}$ sites due to the strong interaction and efficient charge transfer between

Pt$_{iso}$ and WO$_3$. Therefore, the SA-Pt/WO$_3$ sensor exhibits a higher response to TEA than to other gases, i.e. high selectivity.

The high sensitivity of SA-Pt/WO$_3$ is attributed to the high activity of the atomically dispersed Pt (II) on WO$_3$. The roles of Pt include chemical sensitization and electronic sensitization effects. On the one hand, interfacial Pt atoms serve as an active site for the formation of adsorbed oxygen which can diffuse along WO$_3$ surface via spillover effect. The addition of Pt also led to the formation of more oxygen vacancies, which can promote the generation of adsorbed oxygen. According to Eq. 5, adsorbed oxygen will consume electrons and result in an increase in resistance. Fig. S17 shows the corresponding resistance values of the sensors at different operating temperatures in air. The resistance of pure WO$_3$ exhibits typical semiconductor characteristics, and the resistance gradually decreases with temperature. Interestingly, the resistance changes of SA-Pt/WO$_3$ and NC-Pt/WO$_3$ are similar to their response, which increase first and then decrease with temperature, and the maximum resistance values appear at 240 °C. Due to less adsorbed oxygen and thinner electron depletion layer, the resistance of pure WO$_3$ is lower. To the Pt-modified WO$_3$, the content of adsorbed oxygen first increases with temperature. However, when the temperature is higher than 240 °C, the formed adsorbed oxygen will desorb, resulting in a decrease of the resistance [79,80]. Because of the atomic dispersion, every Pt (II) is exposed and forms active sites. SA-Pt/WO$_3$ have a higher number of active sites than NC-Pt/WO$_3$. Therefore, the adsorbed oxygen content of SA-Pt/WO$_3$ should be higher than NC-Pt/WO$_3$, which is consistent with the XPS results. In addition, Pt$_{iso}$ can well bond to their local environment, resulting in relatively weak adsorption to TEA molecules. However, platinum atoms on the clusters/nanoparticles, Pt$_{ox}$, may interact with TEA more strongly. Compared with SA-Pt/WO$_3$, the number of Pt$_{ox}$ is higher on the surface of NC-Pt/WO$_3$, which is indicated by the DRIFTS and STEM results. Therefore, SA-Pt/WO$_3$ is expected to have higher activity for TEA conversion than NC-Pt/WO$_3$, as shown in Fig. 4 c and d. High adsorbed oxygen content and low
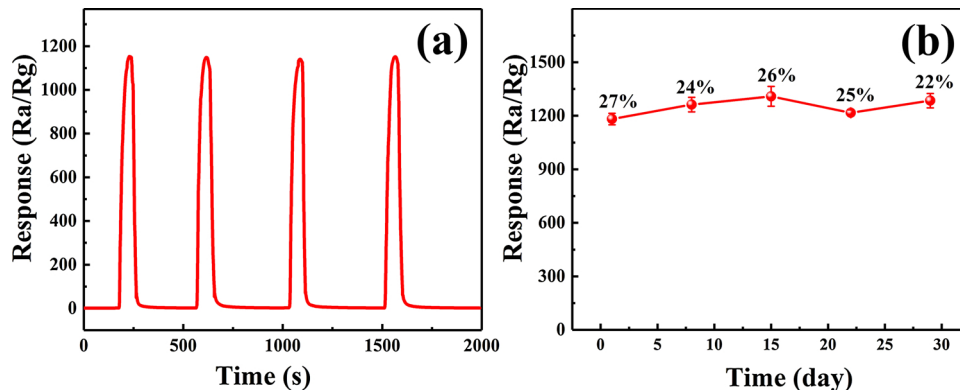

Fig. 7. (a) Response and recovery cycle curves of the SA-Pt/WO$_3$ to 50 ppm TEA, (b) Stability testing results (the value next to the point is the humidity during the measurement process).
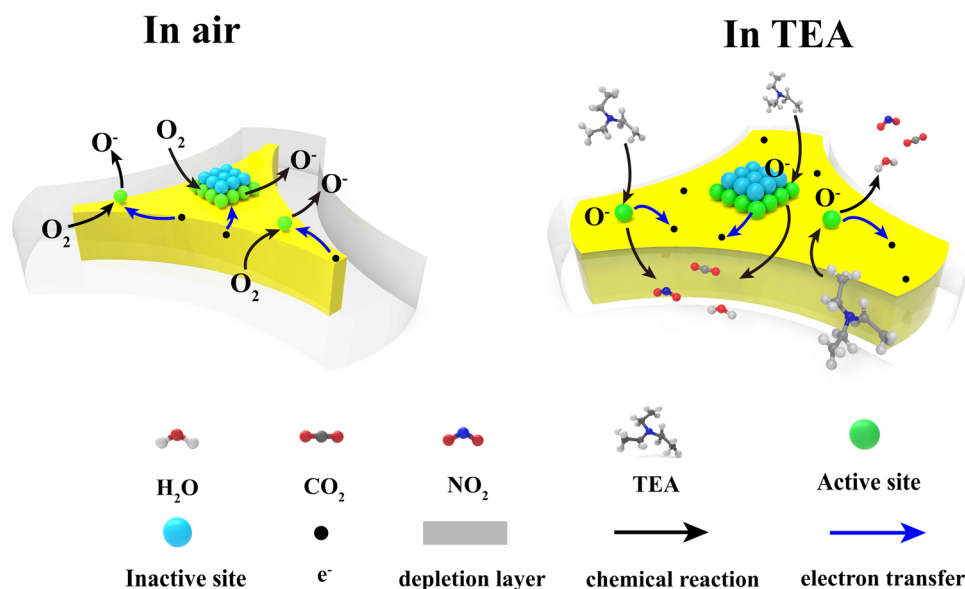
Fig. 8. Schematic illustration for the TEA sensing and conversion mechanism on Pt/WO₃.

activation energy also improve the sensitivity of SA-Pt/WO₃.

Moreover, Pt has electronic sensitization effect. Atomically dispersed Pt (II) can bond with oxygen. PtO and WO₃ are p-type and n-type, respectively. To Pt-modified WO₃, electrons can be transferred by the formation of the p-n junctions. In addition, the work functions of Pt (5.65 eV) and WO₃ (4.56 eV) are different, which leads to the formation of Schottky barrier and caused the electron transfer. The electron transfer will result in the formation of the thick electron depletion layer, significant resistance change and high sensing response [60,81].

The electronic properties of MOS are closely related to their sensing performance, and efficient electron transfer is conducive to the gas response. The electronic characteristics of the sensors were studied using the Hall effect measurements, and the results are shown in Fig. S18. SA-Pt/WO₃ has higher electron mobility than other samples. The narrower band gap of SA-Pt/WO₃ is more conducive to electron transport, thereby increases the electron mobility. The higher electron mobility of SA-Pt/WO₃ allows electrons to transfer efficiently, which benefits the resistance change and sensing performance [82]. The electron concentrations are closely related to the adsorbed oxygen content. As shown in Eq. 5, O₂ captures electrons and forms adsorbed oxygen. This process causes the decrease of the electron concentration [83]. The lower electron concentration of SA-Pt/WO₃ can be attributed to the formation of more adsorbed oxygen due to the larger number of Pt$_{iso}$ sites. In summary, atomically dispersed Pt (II) on WO₃ increases the number of active sites for adsorbed oxygen. High adsorbed oxygen content and low reaction activation energy render SA-Pt/WO₃ a highly efficient sensor and oxidation catalyst of TEA.

4. Conclusions

A highly selective TEA sensor based on atomically dispersed Pt (II) on WO₃ is reported and first fabricated in this work. Atomically dispersed Pt (II) increases the number of active sites for adsorbed oxygen and decreases the activation energy. The high content of adsorbed oxygen and low activation energy are expected to result in complete oxidation of TEA and a significant change of the resistance of SA-Pt/WO₃ at low temperatures. Indeed, we have demonstrated that EG-Pt/WO₃ exhibited very high sensitivity (28.37 ppm^{-1}) and ultra-low detection limit (0.18 ppb) to triethylamine. Selective adsorption on the uniform single Pt (II) sites explains the results. Our experimental test results show that the synthesized 3DOM SA-Pt/WO₃ can also be used for rapid and sensitive monitoring of fish freshness through the catalytic

conversion of TEA. This work provides a novel strategy for the fabrication of highly selective and highly sensitive TEA sensors by stabilizing precious metals on their surfaces at the atomic scale, which is also of potential interest to applications in the design and development of novel catalysts for environmental applications.

Appendix A. Supplementary data

Supplementary material related to this article can be found, in the online version, at doi:https://doi.org/10.1016/j.apcatb.2019.117809.

References

[1] M.H. Chen, C.C. Lai, H.L. Chen, Y.H. Lin, K.Y. Huang, C.H. Lin, H.T. Hsiao, L.C. Liu, C.M. Chen, Mater. Sci. Semicond. Process. 88 (2018) 132–138.
[2] Y. Cui, Z. Chen, X. Liu, Prog. Org. Coat. 100 (2016) 178–187.
[3] G. Brahmachari, N. Nayek, K. Nurjamal, I. Karmakar, S. Begam, Synthesis 50 (2018) 4145–4164.
[4] J.B. Essner, G.A. Baker, Anal. Bioanal. Chem. 410 (2018) 4607–4613.
[5] D.X. Ju, H.Y. Xu, Z.W. Qiu, Z.C. Zhang, Q. Xu, J. Zhang, J.Q. Wang, B.Q. Cao, ACS Appl. Mater. Interfaces 7 (2015) 19163–19171.
[6] B. Gandu, K. Sandhya, A. Gangagni Rao, Y.V. Swamy, Bioresour. Technol. 139 (2013) 155–160.
[7] R. Romero-Gonzalez, M.I. Alarcon-Flores, J.L. Martinez Vidal, A. Garrido Frenich, J. Agric. Food Chem. 60 (2012) 5324–5329.
[8] S. Bourigua, S. El Ichi, H. Korri-Youssoufi, A. Maaref, S. Dzyadevych, N. Jaffrezic Renault, Biosens. Bioelectron. 28 (2011) 105–111.
[9] M. Weber, J.H. Kim, J.H. Lee, J.Y. Kim, I. Iatsunskyi, E. Coy, M. Drobek, A. Julbe, M. Bechelany, S.S. Kim, ACS Appl. Mater. Interfaces 10 (2018) 34765–34773.
[10] M. Weber, J.Y. Kim, J.H. Lee, J.H. Kim, I. Iatsunskyi, E. Coy, P. Miele, M. Bechelany, S.S. Kim, J. Mater. Chem. A Mater. Energy Sustain. 7 (2019) 8107–8116.
[11] Y. Zhu, Y. Zhao, J. Ma, X. Cheng, J. Xie, P. Xu, H. Liu, H. Liu, H. Zhang, M. Wu, A.A. Elzatahry, A. Alghamdi, Y. Deng, D. Zhao, J. Am. Chem. Soc. 139 (2017) 10365–10373.
[12] T. Ueda, T. Maeda, Z. Huang, K. Higuchi, K. Izawa, K. Kamada, T. Hyodo, Y. Shimizu, Sens. Actuators B Chem. 273 (2018) 826–833.
[13] B. Chen, Z. Zhang, M. Baek, S. Kim, W. Kim, K. Yong, Appl. Catal. B 237 (2018) 763–771.
[14] H. Gong, Y. Zhang, Y. Cao, M. Luo, Z. Feng, W. Yang, K. Liu, H. Cao, H. Yan, Appl. Catal. B 237 (2018) 309–317.
[15] K. Sayama, H. Hayashi, T. Arai, M. Yanagida, T. Gunji, H. Sugihara, Appl. Catal. B 94 (2010) 150–157.
[16] T. Gunji, A.J. Jeevagan, M. Hashimoto, T. Nozawa, T. Tanabe, S. Kaneko,

M. Miyauchi, F. Matsumoto, Appl. Catal. B 181 (2016) 475–480.

[17] Y. Ren, Q. Xu, X. Zheng, Y. Fu, Z. Wang, H. Chen, Y. Weng, Y. Zhou, Appl. Catal. B 231 (2018) 381–390.

[18] S.S. Kalanur, I. Yoo, K. Eom, H. Seo, J. Catal. 357 (2018) 127–137.

[19] D. Kim, J. Jang, W. Koo, S. Choi, S. Kim, I. Kim, Sens. Actuators B Chem. 259 (2018) 616–625.

[20] F. Cui, W. Chen, L. Jin, H. Zhang, Z. Jiang, Z. Song, J. Mater., Sci.: Mater. Electron. 29 (2018) 19697–19709.

[21] Y.M. Hunge, A.A. Yadav, S.B. Kulkarni, V.L. Mathe, Sens. Actuators B Chem. 274 (2018) 1–9.

[22] A. Ali Haidry, L. Sun, B. Saruhan, A. Plecenik, T. Plecenik, H. Shen, Z. Yao, Sens. Actuators B Chem. 274 (2018) 10–21.

[23] H. Chen, Y. Zhao, L. Shi, G.D. Li, L. Sun, X. Zou, ACS Appl. Mater. Interfaces 10 (2018) 29795–29804.

[24] S. Sanze, A. Gurlo, C. Hess, Angew. Chem. 52 (2013) 3607–3610.

[25] N.D. Hoa, C.M. Hung, N. Van Duy, N. Van Hieu, Sens. Actuators B Chem. 273 (2018) 784–793.

[26] S. Corby, L. Francas, S. Selim, M. Sachs, C. Blackman, A. Kafizas, J.R. Durrant, J. Am. Chem. Soc. 140 (2018) 16168–16177.

[27] I. Grigioni, M. Abdellah, A. Corti, M.V. Dozzi, L. Hammarstrom, E. Selli, J. Am. Chem. Soc. 140 (2018) 14042–14045.

[28] M. Kobayashi, A. Morita, M. Ikeda, Appl. Catal. B 71 (2007) 94–100.

[29] F.J.P. Schott, P. Balle, J. Adler, S. Kureti, Appl. Catal. B 87 (2009) 18–29.

[30] Y. Su, Z. Han, L. Zhang, W. Wang, M. Duan, X. Li, Y. Zheng, Y. Wang, X. Lei, Appl. Catal. B 217 (2017) 108–114.

[31] X. Liu, H. Zhai, P. Wang, Q. Zhang, Z. Wang, Y. Liu, Y. Dai, B. Huang, X. Qin, X. Zhang, Catal. Sci. Technol. 9 (2019) 652–658.

[32] T. Arai, M. Yanagida, Y. Konishi, A. Ikura, Y. Iwasaki, H. Sugihara, K. Sayama, Appl. Catal. B 84 (2008) 42–47.

[33] X. Yan, M. Xia, B. Xu, J. Wei, B. Yang, G. Yang, Appl. Catal. B 232 (2018) 481–491.

[34] B. Lee, Y. Chen, D. Fu, H.T. Yi, K. Czelen, H. Najafov, V. Podzorov, Nat. Mater. 12 (2013) 1125–1129.

[35] V. Singh, T. Zens, J. Hu, J. Wang, J.D. Musgraves, K. Richardson, L.C. Kimerling, A. Agarwal, Sens. Actuators B Chem. 185 (2013) 195–200.

[36] X. Zhou, X. Cheng, Y. Zhu, A.A. Elzatahry, A. Alghamdi, Y. Deng, D. Zhao, Chin. Chem. Lett. 29 (2018) 405–416.

[37] T. Wagner, S. Haffer, C. Weinberger, D. Klaus, M. Tiemann, Chem. Soc. Rev. 42 (2013) 4036–4053.

[38] S. Li, Y. Diao, Z. Yang, J. He, J. Wang, C. Liu, F. Liu, H. Lu, X. Yan, P. Sun, G. Lu, Sens. Actuators B Chem. 276 (2018) 526–533.

[39] Z. Wang, S. Huang, G. Men, D. Han, F. Gu, Sens. Actuators, B 262 (2018) 577–587.

[40] H.J. Cho, V.T. Chen, S. Qiao, W.T. Koo, R.M. Penner, I.D. Kim, ACS Sens. 3 (2018) 2152–2158.

[41] C. Zhang, F. Liu, Y. Zhai, H. Ariga, N. Yi, Y. Liu, K. Asakura, M. Flytzani-Stephanopoulos, H. He, Angew. Chem. Int. Ed. 51 (2012) 9628–9632.

[42] Y. Peng, Z. Geng, S. Zhao, L. Wang, H. Li, X. Wang, X. Zheng, J. Zhu, Z. Li, R. Si, J. Zeng, Nano Lett. 18 (2018) 3785–3791.

[43] P. Liu, Y. Zhao, R. Qin, S. Mo, G. Chen, L. Gu, D.M. Chevrier, P. Zhang, Q. Guo, D. Zang, Science 352 (2016) 797–800.

[44] A. Wang, J. Li, T. Zhang, Int. Rev. Chem. Eng. 2 (2018) 65–81.

[45] X. Wang, W. Chen, L. Zhang, T. Yao, W. Liu, Y. Lin, H. Ju, J. Dong, L. Zheng, W. Yan, J. Am. Chem. Soc. 139 (2017) 9419–9422.

[46] L. Lin, W. Zhou, R. Gao, S. Yao, X. Zhang, W. Xu, S. Zheng, Z. Jiang, Q. Yu, Y.W. Li, C. Shi, X.D. Wen, D. Ma, Nature 544 (2017) 80–83.

[47] J. Liu, F. R. L, M. Yan g, S. Lee, M. D. M, A.J. Therrien, C.T. Williams, E.C.H. Sykes, M. Flytzani-Stephanopoulos, J. Am. Chem. Soc. 138 (2016) 6396–6399.

[48] B.C. Gates, M. Flytzani-Stephanopoulos, A. David, Dixon Alexander Katz Catal. Sci. Technol. 7 (2017) 4259–4275.

[49] M. Flytzani-Stephanopoulos, B.C. Gates, Annu. Rev. Chem. Biomol. Eng. 3 (2012)

[50] M. Flytzani-Stephanopoulos, Chinese J. Catal. 38 (2017) 1432–1442.

[51] B. Zugic, D.C. Bell, M. Flytzani-Stephanopoulos, Appl. Catal. B 144 (2014) 243–251.

[52] L. Wang, W. Zhang, S. Wang, Z. Gao, Z. Luo, X. Wang, R. Zeng, A. Li, H. Li, M. Wang, X. Zheng, J. Zhu, W. Zhang, C. Ma, R. Si, J. Zeng, Nat. Commun. 7 (2016) 14036.

[53] F.R. Lucci, J. Liu, M.D. Marcinkowski, M. Yang, L.F. Allard, M. Flytzani-Stephanopoulos, E.C. Sykes, Nat. Commun. 6 (2015) 8550.

[54] A. Stein, F. Li, N.R. Denny, Chem. Mater. 20 (2007) 649–666.

[55] H. Li, L. Zhang, H. Dai, H. He, Inorg. Chem. 48 (2009) 4421–4434.

[56] M. Tasbihi, F. Fresno, U. Simon, I.J. Villar-García, V. Pérez-Dieste, C. Escudero, V.A. de la Peña O'Shea, Appl. Catal. B 239 (2018) 68–76.

[57] Z. Qiu, X. Tian, Y. Li, Y. Zeng, C. Fan, M. Wang, Z. Hua, J. Mater. Sci. Mater. Electron. 29 (2018) 11336–11344.

[58] K.J. Lethy, D. Beena, R. Vinod Kumar, V.P. Mahadevan Pillai, V. Ganesan, V. Sathe, Appl. Surf. Sci. 254 (2008) 2369–2376.

[59] Q. Jia, H. Ji, P. Gao, X. Bai, Z. Jin, J. Mater. Sci. Mater. Electron. 26 (2015) 5792–5802.

[60] J. Ma, Y. Ren, X. Zhou, L. Liu, Y. Zhu, X. Cheng, P. Xu, X. Li, Y. Deng, D. Zhao, Adv. Funct. Mater. 28 (2018) 1705268.

[61] J. Wang, X. Zhao, N. Lei, L. Li, L. Zhang, S. Xu, S. Miao, X. Pan, A. Wang, T. Zhang, ChemSusChem 9 (2016) 784–790.

[62] Z. Wang, X. Fan, D. Han, F. Gu, Nanoscale 8 (2016) 10622–10631.

[63] C. Lamberti, A. Zecchina, E. Groppo, S. Bordiga, Chem. Soc. Rev. 39 (2010) 4951–5001.

[64] J.C. Matsubu, V.N. Yang, P. Christopher, J. Am. Chem. Soc. 137 (2015) 3076–3084.

[65] L. DeRita, S. Dai, K. Lopez-Zepeda, N. Pham, G.W. Graham, X. Pan, P. Christopher, J. Am. Chem. Soc. 139 (2017) 14150–14165.

[66] Y. Wang, H. Arandiyan, J. Scott, M. Akia, H. Dai, J. Deng, K.-F. Aguey-Zinsou, R. Amal, ACS Catal. 6 (2016) 6935–6947.

[67] G. Huang, E. He, Z. Wang, H. Fan, J. Shangguan, E. Croiset, Z. Chen, I Ind. Eng. Chem. Res. 54 (2015) 8469–8478.

[68] X.L. Yang, R. Gao, W.-L. Dai, K. Fan, J. Phys. Chem. C 112 (2008) 3819–3826.

[69] Y. Liu, Y. Liu, Y. Zhang, Appl. Catal., B l 242 (2019) 100–108.

[70] Z. Wang, J. Xue, D. Han, F. Gu, ACS Appl. Mater. Interfaces 7 (2015) 308–317.

[71] J. Hassinen, J. Kauppila, J. Leiro, A. Maattanen, P. Ihalainen, J. Peltonen, J. Lukkari, Anal. Bioanal. Chem. 405 (2013) 3611–3617.

[72] J. Wu, K. Tao, Y. Guo, Z. Li, X. Wang, Z. Luo, S. Feng, C. Du, D. Chen, J. Miao, L.K. Norford, Adv. Sci. 4 (2017) 1600319–1600328.

[73] J. Wu, K. Tao, J. Zhang, Y. Guo, J. Miao, L.K. Norford, J J. Mater. Chem. A 4 (2016) 8130–8140.

[74] Z. Wang, H. Zhou, D. Han, F. Gu, J. Mater. Chem. C Mater. Opt. Electron. Devices 5 (2017) 3254–3263.

[75] M.R. Alenezi, A.S. Alshammari, K.D. Jayawardena, M.J. Beliatis, S.J. Henley, S.R. Silva, J. Phys. Chem. C 117 (2013) 17850–17858.

[76] M. D'Arienzo, L. Armelao, C.M. Mari, S. Polizzi, R. Ruffo, R. Scotti, F. Morazzoni, J. Am. Chem. Soc. 133 (2011) 5296–5304.

[77] J. Cao, Y. Xu, L. Sui, X. Zhang, S. Gao, X. Cheng, H. Zhao, L. Huo, Sens. Actuators B Chem. 220 (2015) 910–918.

[78] L. Zhu, M. Wang, T. Kwan Lam, C. Zhang, H. Du, B. Li, Y. Yao, Sens. Actuators B Chem. 236 (2016) 646–653.

[79] J. Wang, Z. Wang, C.J. Liu, ACS Appl. Mater. Interfaces 6 (2014) 12860–12867.

[80] Y. Wang, B. Liu, S. Xiao, X. Wang, L. Sun, H. Li, W. Xie, Q. Li, Q. Zhang, T. Wang, ACS Appl. Mater. Interfaces 8 (2016) 9674–9683.

[81] M. Kim, J. Jang, W. Koo, S. Choi, S. Kim, D. Kim, I. Kim, ACS Appl. Mater. Interfaces 10 (2018) 20643–20651.

[82] Z. Wang, L. Huang, X. Zhu, X. Zhou, L. Chi, Adv. Mater. 29 (2017) 1703192.

[83] J.Y. Lin, W.M. Xie, X.L. He, H.C. Wang, Appl. Phys. A 122 (2016) 801–807.